ENVIRONMENTAL STUDIES

Acceleration of phosphorus weathering under warm climates

Licheng Guo[1]*, Shangfa Xiong[1,2]*, Benjamin J. W. Mills[3], Terry Isson[4], Shiling Yang[1,2], Jingyi Cui[1,2], Yongda Wang[1], Lei Jiang[1,2], Zhifang Xu[1,2], Chunfang Cai[1,2], Yinan Deng[5], Guangyi Wei[6], Mingyu Zhao[1]*

The release of phosphorous (P) via chemical weathering is a vital process that regulates the global cycling of numerous key elements and shapes the size of the Earth's biosphere. It has long been postulated that global climate should theoretically play a prominent role in governing P weathering rates. Yet, there is currently a lack of direct evidence for this relationship based on empirical data at the global scale. Here, using a compilation of temperature and P content data of global surface soils (0 to 30 cm), we demonstrate that P release does enhance at high mean annual surface temperatures. We propose that this amplification of nutrient supply with warming is a critical component of Earth's natural thermostat, and that this relationship likely caused expanded oceanic anoxia during past climate warming events. The potential acceleration of phosphorus loss from soils due to anthropogenic climate warming may pose threats to agricultural production, terrestrial and marine ecosystems, and alter marine redox landscapes.

INTRODUCTION

Phosphorus (P) is one of most important building blocks for life, as it is an essential component for genetic material, adenosine triphosphate, and cell membranes. P is also thought to be the ultimate limiting nutrient for marine primary productivity and thus determines the size of the marine biosphere (*1*). The dissolution of phosphorus-bearing minerals (predominantly apatite) during terrestrial silicate weathering is the single most important source of phosphorus for terrestrial and marine ecosystems (*2*, *3*). Thus, understanding the relationships between environment forcings and terrestrial P weathering intensity is important for our quantitative understanding of the operation of the globally coupled carbon, phosphorus, and oxygen cycles.

Climate is widely believed to have a notable influence on phosphorus weathering based on studies of modern soil P contents (*4*–*6*). As a result, several relationships between temperature and P weathering have been applied in global models to understand the operation of coupled biogeochemical cycles through Earth history, especially during past oceanic anoxia and climate warming events (*7*–*10*). For instance, the Arrhenius equation has been used to describe the effect of temperature on apatite dissolution and P weathering (*7*). The temperature response of P weathering in previous studies is typically inferred from the temperature responses of silicate weathering, carbonate weathering, and oxidation of organic matter, based on an assumed theoretical coupling of P weathering with these three processes (*8*–*10*). However, a quantitative understanding of the relationship between climate and P weathering based on empirical data is still lacking.

Here, using a comprehensive compilation of the mean annual temperature (MAT), chemical index of alteration (CIA), and P contents of global surface soils (0 to 30 cm), we investigate the relationship between climate and P liberation during weathering. We find that P_2O_5/TiO_2 molar ratio of soil is lower under high chemical weathering intensity associated with warmer temperatures. We further quantify the relationship between temperature and P weathering through the incorporation of a global latitudinal temperature gradient in a mathematical model. The results demonstrate that the amplification of P weathering under warm climates is likely a key driver for the development of widespread oceanic anoxia during climate warming events throughout Earth's history.

RESULT

A notable decrease in phosphorus content of soils at temperatures >12°C

A geochemical dataset (n = 14,322; see fig. S1 and Supplementary Text for data distribution) of the major element concentrations of global surface soils was newly compiled to calculate the CIA (see Materials and Methods for a detailed description of the calculation) (*11*). Geochemical records show that fresh minerals and rocks (for example, K-feldspars, plagioclase, granites, granodiorites, and basalts) have CIA values of ~30 to 55 and that CIA values of soils are very close to 100 in extreme weathering environments (*11*, *12*). Thus, the degree of chemical weathering was divided into incipient (CIA = 50 to 60), intermediate (CIA = 60 to 80), and extreme (CIA > 80) stages (*12*). For the application of CIA, the tightly clustered data and the overlapped ranges of the element concentration determined by different analytical techniques (fig. S3), together with the CaO calibration procedure (see Materials and Methods), suggest that the results obtained using different analytical techniques are acceptable for bulk data analysis at the global scale.

The spatial heterogeneity of total P in the 0- to 30-cm layer of global soils displays an increase with latitude (*6*). While P is a soluble

[1]Key Laboratory of Cenozoic Geology and Environment, Institute of Geology and Geophysics, Chinese Academy of Sciences, Beijing, China. [2]College of Earth and Planetary Sciences, University of Chinese Academy of Sciences, Beijing, China. [3]School of Earth and Environment, University of Leeds, Leeds, UK. [4]Environmental Research Institute, University of Waikato, Tauranga, New Zealand. [5]Key Laboratory of Marine Mineral Resources, Ministry of Natural Resources, Guangzhou Marine Geological Survey, China Geological Survey, Guangzhou, China. [6]School of Earth Sciences and Engineering, and Frontiers Science Center for Critical Earth Material Cycling, Nanjing University, Nanjing, China.
*Corresponding author. Email: guolicheng05@mail.iggcas.ac.cn (L.G.); xiongsf@mail.iggcas.ac.cn (S.X.); mingyu.zhao@mail.iggcas.ac.cn (M.Z.)

element, titanium (Ti) is a conservative (immobile) element during chemical weathering (*13*). As a result, element/Ti ratios are commonly used as a proxy for element migration (and release) during silicate weathering (*14*, *15*). Thus, we propose that spatial variations in P_2O_5/TiO_2 (phosphorous weathering intensity) offer useful insight into the migration of P in environments with different silicate weathering intensities. Our results reveal a clear decrease in the molar ratios of soil P_2O_5/TiO_2 with increasing global MAT (Fig. 1A), with notable changes in the temperature dependence (slope) at ~12°C and 20°C.

Next, we compare our results of phosphorous weathering intensity to that of silicate weathering intensity. On a global scale, our dataset also shows that the molar ratios of P_2O_5/TiO_2 are high and relatively stable for CIA = 45 to 80 (the incipient to intermediate weathering stage) with a slight decrease in the CIA range of 70 to 80, while the molar ratios gradually decrease following an increase in CIA in the range of 80 to 100 (Fig. 1B), which is also supported by a K_2O-free CIA (fig. S4). This suggests that P is largely retained in soils when the silicate weathering intensity is weak or moderate (CIA = 45 to 80), and there is less P retention in soils with high silicate weathering intensity (CIA = 80 to 100). Overall, our data reveals a strong nonlinear response of phosphorus liberation to temperature under warmer climates (with an inflection at temperatures ~12°C and CIA ~80). We assess other factors that may play a role in P mobility in fig. S5. These are temperature, precipitation, runoff, biome, lithology, elevation, and slope. We find that the main regulators of P mobility are climatic factors (mainly temperature), although the contribution from nonclimatic factors (e.g., biome, lithology, elevation, and slope) could also be substantial (see Supplementary Text for potential factors controlling P mobility).

DISCUSSION

Effects of soil pH and clay minerals on phosphorus retention

Soil pH likely plays a crucial role in interacting with the intensity of silicate weathering (also expressed as CIA) and, in turn, P liberation. In weathering limited environments with CIA values at <80, there is abundant weatherable material available for water-rock interactions (*16*), due partially to cooler temperatures and a corresponding weak hydrological cycle. In this case, ionic migration during silicate weathering is weak, resulting in relatively high soil pH and alkaline soil environment (Fig. 2A). In contrast, areas with high silicate weathering intensity are characterized by stronger pedogenesis with an intensified hydrological cycle, which elevates the delivery of H^+ and results in lower pH values (Fig. 2A). Elevated H^+ concentration promotes mineral dissolution and the leaching of mobile cations (e.g., Na^+, Ca^{2+}, and K^+), which ultimately increases the soil CIA value (*17*). Fluorapatite [$Ca_5(PO_4)_3F$] and carbonate fluorapatite [$Ca_{9.54}Na_{0.33}Mg_{0.13}(PO_4)_{4.8}(CO_3)_{1.2}F_{2.48}$] dissolution rates increase prominently with decreasing pH (Fig. 2B) (*7*, *18*). Furthermore, lower soil pH values are observed in regions adorned with lush vegetation, as their roots, along with mycorrhizal hyphae, secrete ample organic acids (*17*). Notably, the production of organic acids in soils is influenced by temperature-driven microbial decomposition of organic matter generated by vegetation (*17*). In addition, beyond the influence of climate and the hydrological cycle, the buffering capacity of the bedrock may exert a stabilizing effect on soil pH. Theoretically, this depends on the precipitation and heat induced by climate. Thus, all else being equal, apatite weathering would be relatively weak in a more alkaline soil environment, consistent with the observation of relatively higher P_2O_5/TiO_2 molar ratios of global surface soils under CIA < 80 (Fig. 1B). The lower soil P contents of extreme chemical weathering environments (Fig. 1B) indicate that apatite removal is enhanced by the integrated effects of low pH and elevated temperature and runoff. Lower soil pH in the high weathering intensity environment favors both the desorption of P from clay minerals such as illite (*19*) and the dissolution of Al, Fe, and Ca phosphates (*7*). In a word, rainfall, temperature, and availability of fresh material set pH, silicate weathering intensity and P release.

A decrease in the adsorption capacity of the clay mineral assemblage (change in relative abundance of different clay species) could be another reason for elevated phosphorus weathering under high temperature (>12°C) and high CIA (>80). The mineralogical data

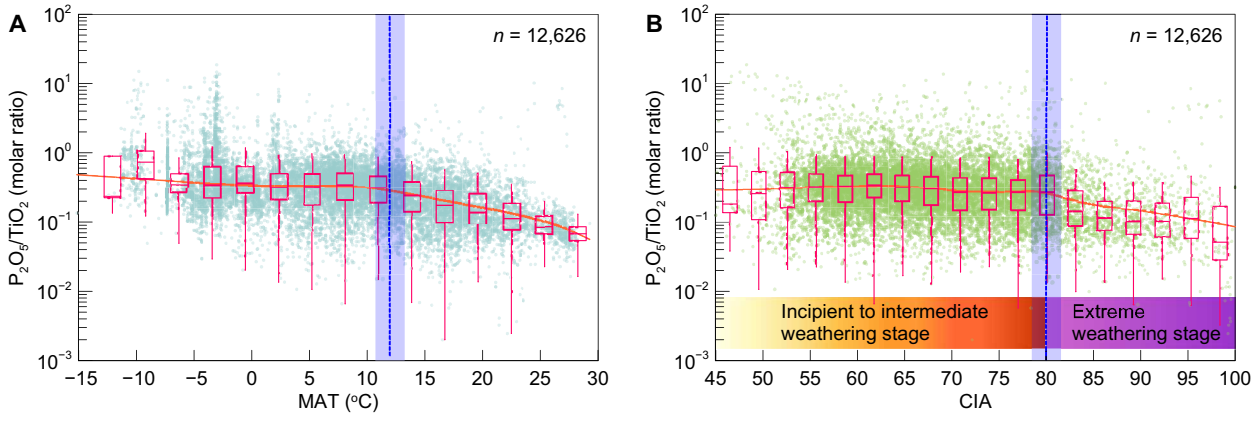

Fig. 1. The relationship between P_2O_5/TiO_2, MAT, and CIA of global surface soil samples (after removal of samples with CIA < 45). (**A**) MAT data are extracted from gridded weather and climate data that documented in the WorldClim database (https://worldclim.org/). These data represent averages for the period spanning 1970 to 2000. (**B**) CIA = 100 × $Al_2O_3/(Al_2O_3 + Na_2O + CaO^* + K_2O)$ (molar ratio), where CaO* represents the amount of CaO incorporated exclusively within the silicate fraction (*11*). Box plots (width of 3°C or 3 CIA units), containing the minimum score, lower quartile, median, upper quartile, and maximum score, depict the P_2O_5/TiO_2 molar ratio of global surface soils (0 to 30 cm). The red curve illustrates locally weighted scatterplot smoothing of the raw data.

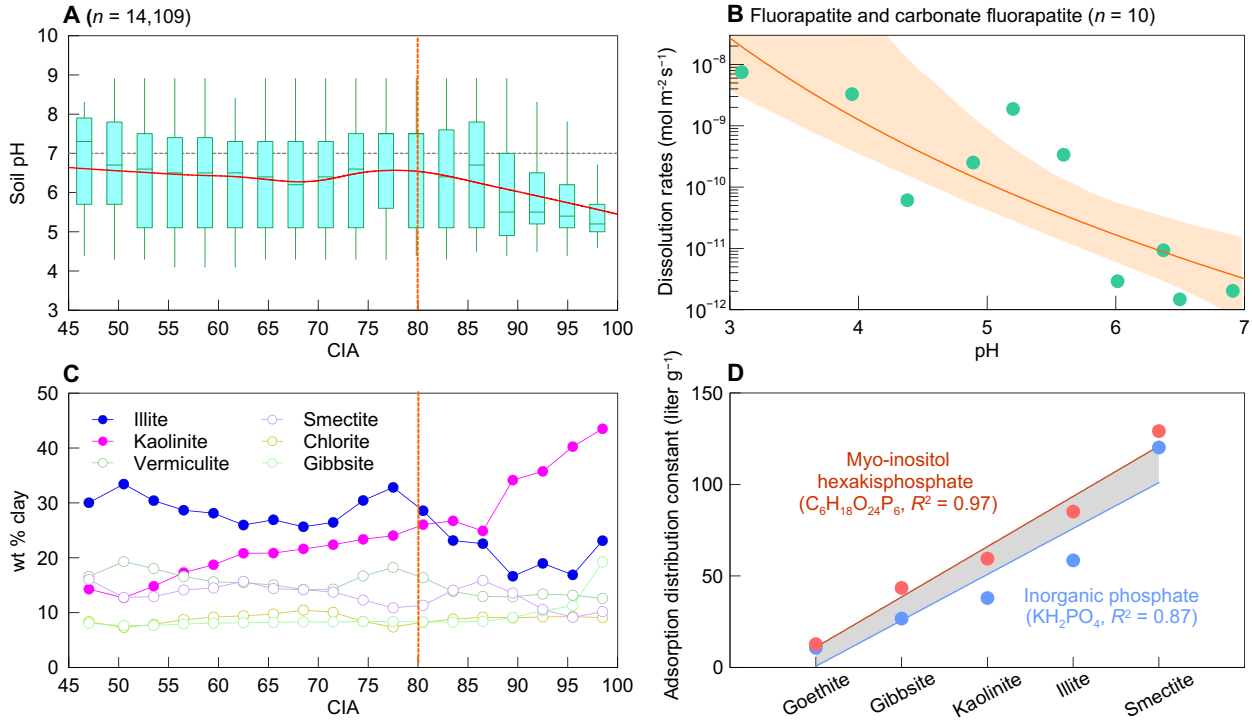

Fig. 2. The mechanism for P loss under warm climatic conditions. (**A**) pH versus CIA for global surface soils (the data are sourced from https://doi.org/10.3334/ORNLDAAC/1247, and the red curve is a locally weighted scatterplot smoothing of the raw data). (**B**) Experimentally determined pH control on fluorapatite and carbonate fluorapatite dissolution rates at 25°C and 1 atm (*7*). The solid line represents the best fit and the shaded region represents the 95% confidence interval. (**C**) CIA versus mineralogy of clay-sized particles in global surface soils (the data are sourced from https://doi.org/10.1594/PANGAEA.868929. Refer to fig. S6 for data plot with 1σ error). The content (wt % clay) means the proportion of each clay mineral group in the total clay content of the soil. (**D**) Adsorption capacity of myo-inositol hexakisphosphate ($C_6H_{18}O_{24}P_6$) and inorganic phosphate (KH_2PO_4) onto different clay minerals and gibbsite (*20*).

from global surface soils shows that illite is abundant in the soil clay fraction when CIA is <80, but kaolinite is more abundant when CIA is >80 (Fig. 2C). Illite has been demonstrated to have a higher adsorption capacity for myo-inositol hexakisphosphate (an organic phosphate) and inorganic phosphate compared to kaolinite (Fig. 2D) (*20*). In sum, soil pH and changes in the adsorption capacity of the clay mineral assemblage (for instance, due to warming) may operate together to trigger the decrease in soil P content in warmer environments with extreme weathering.

A conceptual model can further explain the above-mentioned reorganization of soil P pools under various weathering regimes (Fig. 3). For the incipient to intermediate weathering stage (Fig. 3A; CIA < 80 and relatively higher pH), sluggish apatite weathering due to elevated soil pH yields a relatively small quantity of $H_2PO_4^-$ and HPO_4^{2-} in soil solution, of which a substantial fraction is absorbed by illite and Fe/Al oxides, or synchronously precipitates to Al, Fe, Ca phosphates. Here, a relatively small quantity of P in soil solution is transformed to organic P. This is supported by the fact that a decrease of soil total P concentration is associated with an increase in organic P/apatite P ratio in the semi-arid and humid climatic conditions around the globe (fig. S7) (*21*). Consequently, a small fraction of soil solution and organic P is moved to watersheds by limited runoff under a weak hydrological cycle and cold conditions, with the majority of P locked in soils. Conversely, when the pH of surface soil is lower under extreme weathering intensity (CIA > 80) (Fig. 3B), abundant $H_2PO_4^-$ and HPO_4^{2-} in soil solution is sourced from the intensive weathering of primary apatite and dissolution of Al, Fe, and Ca phosphates, but only a smaller fraction of the total P liberated from weathering is bound to secondary clay (linked to a higher kaolinite/illite ratio). Ultimately, warming-induced intensification of the hydrological cycle in extreme weathering conditions should cause multiple mechanisms for the release of $H_2PO_4^-$ and HPO_4^{2-} from soils to the watershed (*22*) and the ocean. Overall, the primary apatite, the adsorbed P by clay minerals, and the total soil P content decrease under the humid and warm environment. Therefore, assuming that all other environmental factors remain equal (e.g., uplift, and erosion), the phosphorus weathering flux is greater at higher temperatures.

Accelerated phosphorus weathering as a driver of oceanic anoxic events

To estimate changes to P weathering flux under anthropogenic climate warming, we determine the relationship between global MAT (GMAT) and P weathering flux based on the data-driven relationships observed in this study and the modern latitudinal distributions of temperature and land area (see Materials and Methods for a more detailed description). The relationship between P weathering flux and GMAT determined in this study is nonlinear (Fig. 4A and fig. S16). We find notable differences between our expression derived based on a large dataset (Fig. 4A) to the theoretical relationships adopted in previous global biogeochemical models (Fig. 4B). The calculated P weathering flux is slightly less responsive to temperature than those of the LOSCAR and COPSE models (*8*, *9*), determined

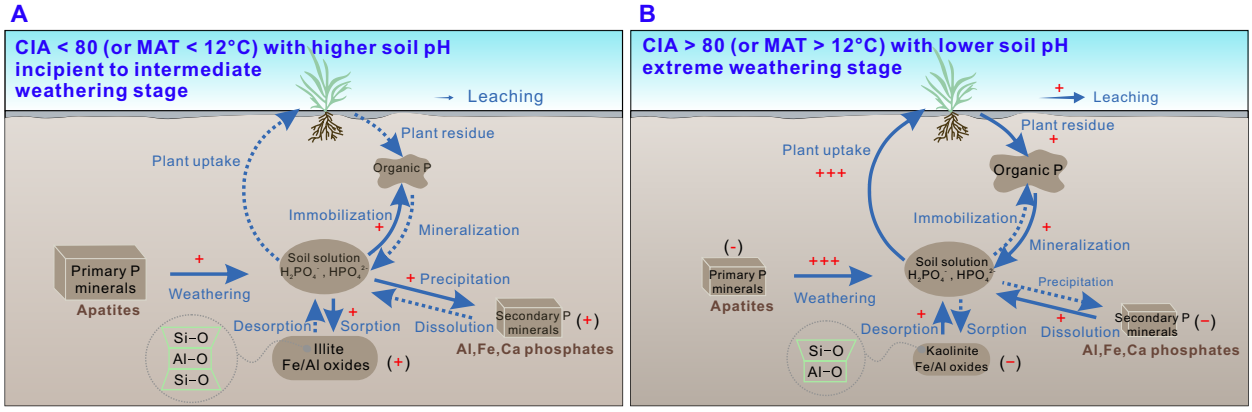

Fig. 3. A schematic diagram for soil phosphorus cycling under various weathering stages. The symbols "+" and "−" show the increases and decreases of the fluxes and reservoirs, respectively. (**A**) Incipient to intermediate weathering stage, with CIA < 80 (or MAT <12°C) and high soil pH. (**B**) Extreme weathering stage, with CIA > 80 (or MAT >12°C) and low soil pH.

based on a global activation energy approach, in the GMAT range of 17° to 20°C. However, our expression increases rapidly in the GMAT range of 20° to 23°C, due to the more complete loss of P at high chemical weathering intensity, which decouples P weathering flux from the weathering of silicates and carbonates. This decoupling effect is clearest when comparing to the SCION model, which has a spatial representation of weathering rates and is arguably therefore much more accurate than COPSE or LOSCAR. The SCION P weathering flux (based predominantly on silicate weathering) tracks the data-driven approach here until a GMAT of about 18°C, after which the new approach shows a much more rapid increase in P weathering flux than is predicted in the model.

Our results support the notion that enhanced P weathering flux could be the main driver for oceanic anoxic events (OAEs) during the Phanerozoic (*9, 23–26*). On the basis of the method described above, we have also calculated the likely shift in P weathering flux during key OAEs of the Mesozoic and Cenozoic (Fig. 4C). The latitudinal distributions of land area during each of these periods are calculated based on the Gplates tectonic reconstructions (*27, 28*). The latitudinal distribution of temperature under each GMAT is interpolated using the results from (*29*). The shifts in GMAT during each of these events are from (*30*) and the references therein (table S1). The model results show that P weathering flux increases 17% ± 10% (2σ), 20% ± 8% (2σ), 33% ± 11% (2σ), and 51% ± 17% (2σ) for OAE1a, OAE2, PETM, and the TOAE, respectively. In particular, our results show that P weathering flux may have increased by 93% ± 20% (2σ) during the Permian-Triassic mass extinction (PT), which is likely sufficient to explain the extent of anoxia during this event (fig. S17) (*23, 26, 31*). Overall, while driving anoxia, accelerated P weathering flux under warming could give rise to strong negative feedback on climate due to its positive effects on primary productivity and organic matter burial (*1*, *7*, *10*). This is also supported by a sensitivity experiment for PT event (fig. S18), which shows that accelerated P weathering flux could ultimately consume a considerable amount of CO_2 from the atmosphere in a timescale of several million years, resulting in a 1° to 2°C reduction in GMAT (fig. S18).

The potential acceleration of phosphorus loss from soils under ongoing anthropogenic driven climate warming may pose threats to agricultural production globally. Such an effect has been observed in modern tropical and subtropics regions. In these regions, soils are typically highly weathered (*32*), resulting in widespread P limitation (*33*) and corresponding requirements for P fertilizer use (*34*). Thus, to maintain agricultural production under warmer climates, it may be necessary to increase P fertilizer use in some areas. Moreover, accelerated transfer of P from soils to the ocean not only generates P limitation for terrestrial ecosystems but also, along with anthropogenic P pollution, boosts marine primary productivity and microbial respiration, increasing the extent of ocean deoxygenation, with potential impacts on marine ecosystems and fisheries. For instance, the works of Watson *et al.* (*35*) predicted that double P weathering flux could lead to severe global ocean deoxygenation on the timeframe of ~1000 years.

MATERIALS AND METHODS

Data compilation

A geochemical dataset (n = 14,322, fig. S1) of the major element concentrations of global surface soils (0 to 30 cm) is compiled from peer-reviewed papers and publicly available reports based on the three criteria. (i) Locations of surface soils that are far (above 10 km) away from industries and villages. (ii) All selected published actual data was determined by chemical analysis and/or instrumental analysis, including x-ray fluorescence (XRF), atomic absorption spectroscopy (AAS), inductively coupled plasma-atomic emission spectrometry (ICP-AES), inductively coupled plasma optical emission spectrometer (ICP-OES), and ICP mass spectrometer. In addition, the disc technique and/or wet chemical dissolution methods (e.g., aqua regia, H_2SO_4-HNO_3-HF mixtures, and HNO_3-HF mixtures) were used in these measurements. (iii) We rejected data with missing values for Al, Ca, Na, or K. A full reference list of the geochemical dataset is provided in the Supplementary Materials (data S1). The geochemical dataset consists of all Al, Ca, Na, and K element concentrations, as well as all or parts of the Si, Fe, Mg, Ti, Mn, and P element concentrations. This dataset differs from the global compilation of modern sediment dataset in the work of Deng *et al.* (*32*), which was mainly from estuaries at the catchment scale, whereas the data points in our dataset are from global surface soils. However, there is a clear positive correlation between climatic factor

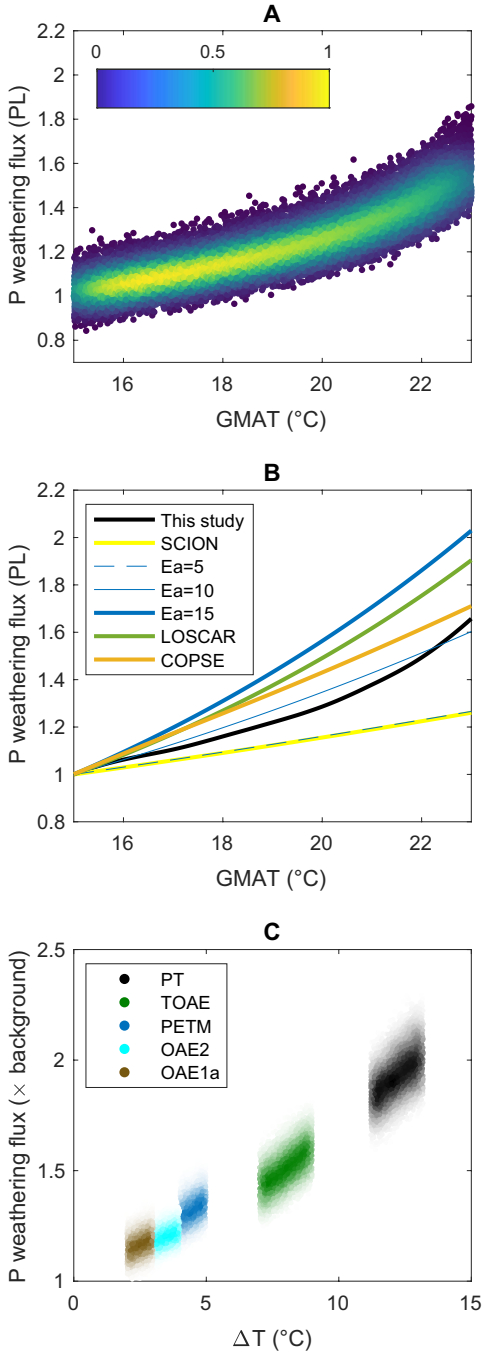

Fig. 4. Model results for variations in P weathering flux with temperature. (**A**) Results from 4×10^4 simulations depicting the intensity of P weathering (relative to the modern GMAT = 15°C) as a function of global MAT (GMAT, °C) under modern conditions. The Monte Carlo calculation is done through sampling P_2O_5/TiO_2 from a 1σ window (0.02) normally distributed around the mean. See Materials and Method for the detailed discussion on this calculation. (**B**) A comparison of the relationship under modern conditions determined in this study with expressions adopted in previous models. Lines with different activation energy (E_a) values (kcal mol^{-1}) are calculated using the Arrhenius equation following (*7*). See Materials and Method for the detailed discussion on this calculation. The results of LOSCAR, COPSE, and SCION model come from the model versions of (*8, 9, 43*), respectively. (**C**) A calculation on the shift of P weathering flux during the OAEs of the Mesozoic and Cenozoic. The Monte Carlo calculation is done through sampling from a 1σ window (0.02) around the calculated mean P_2O_5/TiO_2 at each temperature using a normal distribution and the shift in temperature using a uniform distribution (10^4 simulations for each event). The intensity of the colors represents the density of points. See Materials and Method for the detailed discussion on this calculation. PT, Permian-Triassic mass extinction event; TOAE, Toarcian oceanic anoxic event; OAE1a, Aptian oceanic anoxic event; OAE2, Cenomanian-Turonian oceanic anoxic event; PETM, Paleocene-Eocene Thermal Maximum; PL, relative to present level.

(temperature) and CIA values, which is similar to the findings of Deng *et al.* (fig. S2) (*32*).

The collected data for the elemental concentrations of Al, K, Na, and P from global surface soils (fig. S3) shows a tightly clustered distribution, and the ranges in element concentrations for Al, Na, K, and P determined by different methods, namely, ICP-AES ($n = 9203$), XRF ($n = 2505$), and AAS ($n = 1667$), are overlapped. This suggests that the results obtained using different analytical techniques are acceptable for bulk data analysis on a global scale.

Chemical weathering index

The CIA (*11*) directly indicates the leaching of mobile cations (e.g., Na^+, Ca^{2+}, and K^+) relative to more stable elements (e.g., Al^{3+}) within soils or sediments. It assumes that the dissolution of plagioclase and potassium feldspar and the concomitant formation of clay minerals (e.g., kaolinite) are the dominant process during chemical weathering (*11*). It is calculated as: CIA = $100 \times Al_2O_3/(Al_2O_3 + Na_2O + CaO^* + K_2O)$ (molar ratio), where CaO* must be the amount of CaO incorporated exclusively within the silicate fraction. Therefore, the content of CaO was evaluated and calibrated to CaO* using the calibration procedure described by (*36*) with an assumption that molar CaO/Na_2O ratio of the silicate fraction is less than or equal to 1. The greatest discrepancies occurring for the CIA values of 60 to 80 is up to ~3 units, which is much smaller than the variability caused by each forcing factor (such as climate, rock type, tectonic activity, diagenesis, and grain-size effects) and can be averaged out across a large scale (*16, 32*). High CIA values indicate the intensive leaching of mobile cations from fresh regolith, when the degree of chemical weathering is extreme (CIA > 80). Conversely, low values correspond to incipient chemical weathering (CIA = 50 to 60).

Calculation of the relationship between temperature and P weathering flux

To predict the potential changes in global P weathering flux under anthropogenic climate warming, we calculate the relationship between global mean surface temperature and P weathering flux based on the relationship between MAT and P weathering intensity observed in this study and the latitudinal distributions of temperature at certain GMAT, as well as the modern latitudinal distribution of land area. Therefore, global P weathering flux (P_w) is calculated as

$$P_w = \sum_{i=1}^{18} A_i * f_{P_{wMAT}}\left[f_{MAT_i}(GMAT)\right] * D \quad (1)$$

where D represents the denudation rate, f_{MATi} is the MAT at latitude band i under certain GMAT (fig. S8), f_{Pw_MAT} is the relationship between P release for given amounts of denudated materials and MAT observed in this study (see fig. S9 for the used relationship), and A_i is the proportion of the land area at each latitude band i (fig. S10). The land area is divided into 18 bands by latitude with a band width of 5°C (e.g., 0° to 5°C of both hemispheres are combined into the same band). The range of GMAT for this calculation is 15° to 23°C. The calculated flux of P weathering is calibrated to the modern value (i.e., with a GMAT of 15°C). We have used a Monte Carlo sampling approach for the calculation of Fig. 4A, through sampling the 1σ error (0.02) in the calculated mean P_2O_5/TiO_2 at each temperature using a normal distribution. The f_{Pw_MAT} is calculated from the relationship between soil P contents and MAT using the following equation

$$f_{Pw\_MAT} = \left[\frac{P_2O_5}{TiO_2}\right]_i - \left[\frac{P_2O_5}{TiO_2}\right]_{MAT} \quad (2)$$

where $\left[\frac{P_2O_5}{TiO_2}\right]_i$ is the initial $\frac{P_2O_5}{TiO_2}$ ratio of the un-weathered parent rocks,which is 0.33 based on the P_2O_5/TiO_2 at the CIA range of 45 to 50 (Fig. 1B). $\left[\frac{P_2O_5}{TiO_2}\right]_{MAT}$ is the $\frac{P_2O_5}{TiO_2}$ ratio of the soils for a given MAT. See the Supplementary Materials for further discussion on Eq. 1.

We have also plotted the relationship between GMAT and P weathering flux used in the previous global biogeochemical models for deep time. In these models, the Arrhenius equation has typically been used to calculate the relationship between GMAT and P weathering flux (*7*)

$$P_w = P_{w\_T_0} * e^{-\left(\frac{E_a}{R*GMAT} - \frac{E_a}{R*T_0}\right)} \quad (3)$$

where P_{w_T0} is the flux of P weathering at certain reference temperature (T_0), E_a the activation energy, and R the universal gas constant.

On the basis of the method described above, we have also calculated the shift in global P weathering flux during the most prominent OAEs (PT, TOAE, OAE1a, OAE2, and PETM) of the Mesozoic and Cenozoic (Fig. 4C) through the application of the shifts in land area and temperature distributions across latitude gradients during each of these periods (figs. S11 and S12). The latitudinal distributions of land area during each of these periods are calculated based on the Gplates tectonic reconstructions (*27, 28*). The latitudinal distribution of temperature under each GMAT is interpolated using the results from (*29*). The shifts in GMAT during each of these events are from (*30*) and the references therein (table S1). In particular, a GMAT shift of 11° to 13°C was inferred for the PT event based on the 8° to 10°C temperature increase in the tropic zone (*37, 38*) and the latitudinal distribution of temperature (*29*). The estimates for the changes in P weathering flux during OAEs are likely conservative as they do not include the enhancement of P weathering flux due to the exposure of fresh basalt for weathering during these events [e.g., (*39*) and references therein].

In this calculation, the denudation rate was kept constant, as no clear relationship exists between erosion and temperature (*40*). This is also supported by our data compilation, which shows no clear global relationship between erosion/denudation rate and temperature (fig. S13; further discussion in Supplementary Text). Overall, this premise enables the use of variations in P_2O_5/TiO_2 of soils to track P weathering rate or flux on a global scale (see Supplementary Text for further discussion). In addition, the erosion/denudation rate is likely primarily controlled by topography (*41*), which distributes approximately randomly around the globe (for data source, refer to Global Mountain Explorer 2.0 at https://rmgsc.cr.usgs.gov/gme/gme.shtml, and the topography during periods of geological history is poorly known. To further verify the validity of our model, we have also calculated the relationship between climate and silicate weathering using a previous relationship between CIA and MAT (fig. S14) (*32*) as well as a method similar to the above calculation, with the results shown in fig. S15. The calculated results (based on the Arrhenius equation) show that the strength of climate control on silicate weathering is equivalent to an E_a value of ~18 kJ mol^{-1}. This compares well with a recent estimate (*42*) of 22 ± 3 kJ mol^{-1}, which thus supports the validity of our method.

Supplementary Materials

This PDF file includes:
Supplementary Text
Figs. S1 to S18
Table S1
Legend for data S1
References

Other Supplementary Material for this manuscript includes the following:
Data S1

REFERENCES AND NOTES

1. T. Tyrrell, The relative influences of nitrogen and phosphorus on oceanic primary production. *Nature* **400**, 525–531 (1999).
2. K. C. Ruttenberg, The Global Phosphorus Cycle, in *Treatise on Geochemistry*, H. D. Holland, K. K. Turekian, Eds. (Elsevier, 2014), pp. 499–558.
3. S. Sharoni, I. Halevy, Rates of seafloor and continental weathering govern Phanerozoic marine phosphate levels. *Nat. Geosci.* **16**, 75–81 (2023).
4. T. W. Walker, J. K. Syers, The fate of phosphorus during pedogenesis. *Geoderma* **15**, 1–19 (1976).
5. K. B. Föllmi, R. Hosein, K. Arn, P. Steinmann, Weathering and the mobility of phosphorus in the catchments and forefields of the Rhône and Oberaar glaciers, central Switzerland: Implications for the global phosphorus cycle on glacial–interglacial timescales. *Geochim. Cosmochim. Acta* **73**, 2252–2282 (2009).
6. X. J. He, L. Augusto, D. S. Goll, B. Ringeval, Y. P. Wang, J. Helfenstein, Y. Y. Huang, K. L. Yu, Z. Q. Wang, Y. C. Yang, E. Q. Hou, Global patterns and drivers of soil total phosphorus concentration. *Earth Syst. Sci. Data* **13**, 5831–5846 (2021).
7. M. W. Guidry, F. T. Mackenzie, Apatite weathering and the Phanerozoic phosphorus cycle. *Geology 28*, 631–634 (2000).
8. N. M. Bergman, T. M. Lenton, A. J. Watson, COPSE: A new model of biogeochemical cycling over Phanerozoic time. *Am. J. Sci.* **304**, 397–437 (2004).
9. N. Komar, R. E. Zeebe, Redox-controlled carbon and phosphorus burial: A mechanism for enhanced organic carbon sequestration during the PETM. *Earth Planet. Sci. Lett.* **479**, 71–82 (2017).
10. M. Y. Zhao, B. J. W. Mills, W. B. Homoky, C. L. Peacock, Oxygenation of the Earth aided by mineral–organic carbon preservation. *Nat. Geosci.* **16**, 262–267 (2023).
11. H. W. Nesbitt, G. M. Young, Early Proterozoic climates and plate motions inferred from major element chemistry of lutites. *Nature* **299**, 715–717 (1982).
12. C. M. Fedo, H. W. Nesbitt, G. M. Young, Unraveling the effects of potassium metasomatism in sedimentary rocks and paleosols, with implications for paleoweathering conditions and provenance. *Geology* **23**, 921–924 (1995).
13. L. G. Woodruff, G. M. Bedinger, N. M. Piatak, Titanium, in *Chaper T of Critical Mineral Resources of the United States—Economic and Environmental Geology and Prospects for Future Supply*, K. J. Schulz, J. H. DeYoung Jr., R. R. Seal II, D. C. Bradley, Eds. (U.S. Geological Survey Professional Paper 1802, 2017), pp. 1–23.
14. S. L. Yang, F. Ding, Z. L. Ding, Pleistocene chemical weathering history of Asian arid and semi-arid regions recorded in loess deposits of China and Tajikistan. *Geochim. Cosmochim. Acta* **70**, 1695–1709 (2006).
15. M. Y. Zhao, Y. F. Zheng, The intensity of chemical weathering: Geochemical constraints from marine detrital sediments of Triassic age in South China. *Chem. Geol.* **391**, 111–122 (2015).
16. L. C. Guo, J. B. Wu, Y. L. Chen, S. F. Xiong, J. Y. Cui, Z. L. Ding, Modern silicate weathering regimes across China revealed by geochemical records from surface soils. *J. Geophys. Res. Earth Surf.* **127**, e2022JF006728 (2022).
17. R. A. Berner, *The Phanerozoic carbon cycle: CO_2 and O_2* (Oxford Univ. Press, 2004), pp. 13–39.
18. M. Peld, K. Tõnsuaadu, V. Bender, Sorption and desorption of Cd^{2+} and Zn^{2+} ions in apatite-aqueous systems. *Environ. Sci. Technol.* **38**, 5626–5631 (2004).
19. N. J. Barrow, The effects of pH on phosphate uptake from the soil. *Plant Soil* **410**, 401–410 (2017).
20. X. D. Yan, *The immobilization effects and mechanism analysis of mineral soil conditioner on nitrogen and phosphorus*, Doctoral Thesis, South China University of Technology, Guangzhou, (2018).
21. E. Q. Hou, C. R. Chen, Y. Q. Luo, G. Y. Zhou, Y. W. Kuang, Y. G. Zhang, M. Heenan, X. K. Lu, D. Z. Wen, Effects of climate on soil phosphorus cycle and availability in natural terrestrial ecosystems. *Glob. Chang. Biol.* **24**, 3344–3356 (2018).
22. A. Mishra, J. K. Tripathi, P. Mehta, V. Rajamani, Phosphorus distribution and fractionation during weathering of amphibolites and gneisses in different climatic setups of the Kaveri river catchment, India. *Appl. Geochem.* **33**, 173–181 (2013).
23. K. M. Meyer, L. R. Kump, A. Ridgwell, Biogeochemical controls on photic-zone euxinia during the end-Permian mass extinction. *Geology* **36**, 747–750 (2008).
24. I. Tsandev, C. P. Slomp, Modeling phosphorus cycling and carbon burial during Cretaceous oceanic anoxic events. *Earth Planet. Sci. Lett.* **286**, 71–79 (2009).
25. C. Winguth, A. M. Winguth, Simulating Permian–Triassic oceanic anoxia distribution: Implications for species extinction and recovery. *Geology* **40**, 127–130 (2012).
26. D. Hülse, K. V. Lau, S. J. van de Velde, S. Arndt, K. M. Meyer, A. Ridgwell, End-Permian marine extinction due to temperature-driven nutrient recycling and euxinia. *Nat. Geosci.* **14**, 862–867 (2021).
27. C. R. Scotese, *PALEOMAP PaleoAtlas for GPlates and the PaleoData Plotter Program*. (PALEOMAP Project, 2016); http://earthbyte.org/paleomap-paleoatlas-for-gplates/.
28. R. D. Müller, J. Cannon, X. D. Qin, R. J. Watson, M. Gurnis, S. Williams, T. Pfaffelmoser, M. Seton, S. H. J. Russell, S. Zahirovic, GPlates: Building a virtual Earth through deep time. *Geochem. Geophys. Geosyst.* **19**, 2243–2261 (2018).
29. C. R. Scotese, H. J. Song, B. J. W. Mills, D. G. van der Meer, Phanerozoic paleotemperatures: The Earth's changing climate during the last 540 million years. *Earth Sci. Rev.* **215**, 103503 (2021).
30. X. M. Hu, J. Li, Z. Han, Y. X. Li, Two types of hyperthermal events in the Mesozoic-Cenozoic: Environmental impacts, biotic effects, and driving mechanisms. *Sci. China Earth Sci.* **63**, 1041–1058 (2020).
31. K. Ozaki, E. Tajika, Biogeochemical effects of atmospheric oxygen concentration, phosphorus weathering, and sea-level stand on oceanic redox chemistry: Implications for greenhouse climates. *Earth Planet. Sci. Lett.* **373**, 129–139 (2013).
32. K. Deng, S. Y. Yang, Y. L. Guo, A global temperature control of silicate weathering intensity. *Nat. Commun.* **13**, 1781 (2022).
33. E. Z. Du, C. Terrer, A. F. A. Pellegrini, A. Ahlstrom, C. J. van Lissa, X. Zhao, N. Xia, X. H. Wu, R. B. Jackson, Global patterns of terrestrial nitrogen and phosphorus limitation. *Nat. Geosci.* **13**, 221–226 (2020).
34. C. Q. Lu, H. Q. Tian, Global nitrogen and phosphorus fertilizer use for agriculture production in the past half century: Shifted hot spots and nutrient imbalance. *Earth Syst. Sci. Data* **9**, 181–192 (2017).
35. A. J. Watson, T. M. Lenton, B. J. W. Mills, Ocean deoxygenation, the global phosphorus cycle and the possibility of human-caused large-scale ocean anoxia. *Philos. Trans. R. Soc. Lond. A* **375**, 20160318 (2017).
36. S. M. McLennan, Weathering and global denudation. *J. Geol.* **101**, 295–303 (1993).
37. M. M. Joachimski, X. L. Lai, S. Z. Shen, H. S. Jiang, G. M. Luo, B. Chen, J. Chen, Y. D. Sun, Climate warming in the latest Permian and the Permian-Triassic Mass extinction. *Geology* **40**, 195–198 (2012).
38. Y. D. Sun, M. M. Joachimski, P. B. Wignall, C. B. Yan, Y. L. Chen, H. S. Jiang, L. N. Wang, X. L. Lai, Lethally hot temperatures during the early Triassic Greenhouse. *Science* **338**, 366–370 (2012).
39. M. Schobben, W. J. Foster, A. R. N. Sleveland, V. Zuchuat, H. H. Svensen, S. Planke, D. P. G. Bond, F. Marcelis, R. J. Newton, P. B. Wignall, S. W. Poulton, A nutrient control on marine anoxia during the end-Permian mass extinction. *Nat. Geosci.* **13**, 640–646 (2020).
40. E. W. Portenga, P. R. Bierman, Understanding Earth's eroding surface with ^{10}Be. *GSA Today* **21**, 4–10 (2011).
41. M. A. Harel, S. M. Mudd, M. Attal, Global analysis of the stream power law parameters based on worldwide ^{10}Be denudation rates. *Geomorphology* **268**, 184–196 (2016).
42. S. L. Brantley, A. Shaughnessy, M. I. Lebedeva, V. N. Balashov, How temperature-dependent silicate weathering acts as Earth's geological thermostat. *Science* **379**, 382–389 (2023).
43. B. J. W. Mills, Y. Donnadieu, Y. Goddéris, Spatial continuous integration of Phanerozoic global biogeochemistry and climate. *Gondw. Res.* **100**, 73–86 (2021).
44. J. Hartmann, N. Moosdorf, R. Lauerwald, M. Hinderer, A. J. West, Global chemical weathering and associated P-release—The role of lithology, temperature and soil properties. *Chem. Geol.* **363**, 145–163 (2014).
45. P. Borrelli, D. A. Robinson, L. R. Fleischer, E. Lugato, C. Ballabio, C. Alewell, K. Meusburger, S. Modugno, B. Schütt, V. Ferro, V. Bagarello, K. V. Oost, L. Montanarella, P. Panagos, An assessment of the global impact of 21st century land use change on soil erosion. *Nat. Commun.* **8**, 2013 (2017).
46. R. M. Dzombak, N. D. Sheldon, Weathering intensity and presence of vegetation are key controls on soil phosphorus concentrations: Implications for past and future terrestrial ecosystems. *Soil Syst.* **4**, 73 (2020).
47. O. A. Chadwick, J. Chorover, K. D. Chadwick, J. B. Bateman, E. W. Slessarev, M. Kramer, A. Thompson, P. M. Vitousek, Constraints of Climate and Age on Soil Development in Hawai'I, in *Biogeochemistry of the Critical Zone*, A. S. Wymore, W. H. Yang, W. L. Silver, W. H. McDowell, J. Chorover, Eds. (Springer Nature, 2022), pp. 49–88.
48. S. Anindita, S. Sleutel, D. Vandenberghe, J. D. Grave, V. Vandenhende, P. Finke, Land use impacts on weathering, soil properties, and carbon storage in wet Andosols, Indonesia. *Geoderma* **423**, 115963 (2022).
49. A. Sako, S. Semdé, U. Wenmenga, Geochemical evaluation of soil, surface water and groundwater around the Tongon gold mining area, northern Côte d'Ivoire, West Africa. *J. Afr. Earth Sci.* **145**, 297–316 (2018).
50. S. F. von Fromm, A. M. Hoyt, M. Lange, G. E. Acquah, E. Aynekulu, A. A. Berhe, S. M. Haefele, S. P. McGrath, K. D. Shepherd, A. M. Sila, J. Six, E. K. Towett, S. E. Trumbore, T.-G. Vågen, E. Weullow, L. A. Winowiecki, S. Doetterl, Continental-scale controls on soil organic carbon across sub-Saharan Africa. *Soil* **7**, 305–332 (2021).

51. J. B. Maynard, Chemistry of modern soils as a guide to interpreting Precambrian paleosols. *J. Geol.* **100**, 279–289 (1992).
52. D. M. Olson, E. Dinerstein, E. D. Wikramanayake, N. D. Burgess, G. V. N. Powell, E. C. Underwood, J. A. D'Amico, I. Itoua, H. E. Strand, J. C. Morrison, C. J. Loucks, T. F. Allnutt, T. H. Ricketts, Y. Kura, J. F. Lamoreux, W. W. Wettengel, P. Hedao, K. R. Kassem, Terrestrial ecoregions of the world: A new map of life on Earth. *Bioscience* **51**, 933–938 (2001).
53. E. J. Tarbuck, F. K. Lutgens, D. G. Tasa, *Applications and Investigations in Earth Science* (Pearson Edcation, 2019).
54. P. Borrelli, C. Alewell, P. Alvarez, J. A. A. Anache, J. Baartman, C. Ballabio, N. Bezak, M. Biddoccu, A. Cerdà, D. Chalise, S. C. Chen, W. Chen, A. M. De Girolamo, G. D. Gessesse, D. Deumlich, N. Diodato, N. Efthimiou, G. Erpul, P. Fiener, M. Freppaz, F. Gentile, A. Gericke, N. Haregeweyn, B. F. Hu, A. Jeanneau, K. Kaffas, M. Kiani-Harchegani, I. L. Villuendas, C. J. Li, L. Lombardo, M. López-Vicente, M. E. Lucas-Borja, M. Märker, F. Matthews, C. Y. Miao, M. Mikoš, S. Modugno, M. Möller, V. Naipal, M. Nearing, S. Owusu, D. Panday, E. Patault, C. V. Patriche, L. Poggio, R. Portes, L. Quijano, M. R. Rahdari, M. Renima, G. F. Ricci, J. Rodrigo-Comino, S. Saia, A. N. Samani, C. Schillaci, V. Syrris, H. S. Kim, D. N. Spinola, P. T. Oliveira, H. F. Teng, R. Thapa, K. Vantas, D. Vieira, J. E. Yang, S. Q. Yin, D. A. Zema, G. J. Zhao, P. Panagos, Soil erosion modelling: A global review and statistical analysis. *Sci. Total Environ.* **780**, 146494 (2021).
55. J. T. Chen, I. P. Montanez, S. Zhang, T. Isson, S. I. Macarewich, N. J. Planavsky, F. F. Zhang, S. Rauzi, K. Daviau, L. Yao, Y. P. Qi, Y. Wang, J. X. Fan, C. J. Poulsen, A. D. Anbar, S. Z. Shen, X. D. Wang, Marine anoxia linked to abrupt global warming during Earth's penultimate icehouse. *Proc. Natl. Acad. Sci. U.S.A.* **119**, e2115231119 (2022).

Acknowledgments: We thank J. B. Wu and S. Liu for data collection. We also thank Z. L. Chen and Z. H. Tang for valuable discussions and suggestions. **Funding:** S.Y. is supported by the National Key R & D Program of China (grant no. 2022YFF0800800), L.G. is funded by Strategy Priority Research Program (Category B) of Chinese Academy of Sciences (grant no. XDB0710000), L.G. and S.X. are funded by the National Natural Science Foundation of China (grant nos. 42007282 and 42077409), M.Z. is funded by the Programme of the Chinese Academy of Sciences (grant nos. E32D530201 and E32C530102), L.G. is funded by the Programme of the Chinese Academy of Sciences (grant no. E351530101), S.Y. is funded by the Key Research Program of the Institute of Geology & Geophysics, Chinese Academy of Sciences (grant no. IGGCAS-201905), and B.J.W.M. is funded by the UK NERC (grant no. NE/S009663/1).
Author contributions: Conceptualization: L.G., M.Z., and S.X.; methodology: L.G. and M.Z.; funding acquisition: L.G., M.Z., S.X., S.Y., and B.J.W.M.; resources: L.G.; investigation: L.G., B.J.W.M., S.Y., J.C., Y.W., L.J., Z.X., C.C., Y.D., and G.W.; formal analysis: L.G., M.Z., T.I., S.Y., Y.W., and Y.D.; data curation: L.G. and M.Z.; software: M.Z. and B.J.W.M.; validation: L.G., M.Z., T.I., and G.W.; visualization: L.G. and T.I.; supervision: M.Z., L.G., and S.X.; project administration: M.Z., L.G., and S.X.; writing–original draft: L.G., M.Z., and B.J.W.M.; writing–review and editing: L.G., M.Z., S.X., T.I., B.J.W.M., and G.W. **Competing interests:** The authors declare that they have no competing interests. **Data and materials availability:** All data needed to evaluate the conclusions in the paper are present in the paper and/or the Supplementary Materials.

Submitted 6 November 2023
Accepted 6 June 2024
Published 10 July 2024
10.1126/sciadv.adm7773